Acta Materialia 180 (2019) 329–340

Contents lists available at ScienceDirect

Acta Materialia

journal homepage: www.elsevier.com/locate/actamat

Full length article

Role of surface oxide layers in the hydrogen embrittlement of austenitic stainless steels: A TOF-SIMS study

Chika Izawa [a], Stefan Wagner [b], Martin Deutges [a], Mauro Martín [c], Sebastian Weber [d], Richard Pargeter [e], Thorsten Michler [f], Haru-Hisa Uchida [g], Ryota Gemma [h], Astrid Pundt [a, b, *]

[a] Institut für Materialphysik der Universität Göttingen, Friedrich-Hund-Platz 1, 37077, Göttingen, Germany
[b] Institut für Angewandte Materialien (IAM-WK), Karlsruher Institut für Technologie (KIT), Engelbert-Arnold-Straße 4, 76131, Karlsruhe, Germany
[c] Institute of Physics Rosario CONICET-UNR, 27 de Febrero 210 Bis, Rosario, Argentina
[d] Bergische Universität Wuppertal, Fakultät für Maschinenbau und Sicherheitstechnik, Lehrstuhl für Neue Fertigungstechnologien und Werkstoffe, Bahnhofstr. 15, 42651, Solingen, Germany
[e] TWI Ltd, Granta Park, Great Abington, Cambridge, CB21 6AL, United Kingdom
[f] Opel Automobile GmbH, 65423, Rüsselsheim, Germany
[g] Department of Human Development, Tokai University, Kitakaname 4-1-1, Hiratsuka, Kanagawa, 259-1292, Japan
[h] Department of Materials Science, Tokai University, Kitakaname 4-1-1, Hiratsuka, Kanagawa, 259-1292, Japan

ARTICLE INFO

Article history:
Received 14 March 2019
Received in revised form
31 July 2019
Accepted 12 September 2019
Available online 14 September 2019

Keywords:
Hydrogen embrittlement
Austenitic stainless steel
Oxide layers
Dislocations
Martensite transformation

ABSTRACT

Hydrogen environment embrittlement (HEE) of low-nickel austenitic stainless steels (AISI 300 series) with different chemical compositions was studied focusing on the impact of the steels surface oxides, grain sizes and dislocation arrangements. The susceptibility of the steels to HEE is judged with respect to the relative reduction of area (RRA), where the HEE susceptibility is lower for larger RRA values.

For many AISI 300 steels a linear trend is observed correlating RRA and the probability of strain induced martensite formation in tensile tests. Some steels, however, depart from the general trend, revealing greater HEE resistances.

A careful examination of possible factors influencing HEE of the investigated steels reveals that high RRA values are linked to a specific type of oxide layer, namely the "high constant level oxide", as categorized by TOF-SIMS evaluation. Thus, this type of oxide layer may be able to lower the steels HEE susceptibility. Other types of surface oxides, grain sizes and dislocation arrangements in the matrix of the particular AISI 300 steels appear to be of secondary importance.

1. Introduction

In an infrastructure utilizing hydrogen as an energy carrier, chromium (Cr)–nickel (Ni) austenitic stainless steels applied in tanks or pipelines are among the materials with the highest resistance against hydrogen environment embrittlement (HEE). However, from an economic point of view the replacement of Cr and Ni is desired for the application of steels. Low-nickel austenitic stainless steels of the AISI 300 series are targeted. As a drawback, the steel's resistance against HEE increases with decreasing nickel content [1–3].

Among a number of factors influencing the susceptibility of low-nickel austenitic stainless steels to HEE [4,5], a general contribution is related to the presence of the martensite phase. When the content of nickel as a strong austenite stabilizer is reduced, an increased tendency to form local, deformation-induced martensite is observed [5–7] for steels that are plastically deformed. Martensite formed at crack tips can serve as a hydrogen diffusion path way into the steel [5,8–10] due to its bcc structure with a carbon-content dependent tetragonal distortion [11]. As the hydrogen solubility of martensite is significantly smaller compared to that of austenite [9], absorbed hydrogen can subsequently be trapped in adjacent austenite grains. There it acts as a defactant ("defect acting agent") [12,13], modifying stacking fault energies and dislocation mobilities due to its adsorption to defect surfaces.

* Corresponding author. Institut für Materialphysik der Universität Göttingen, Friedrich-Hund-Platz 1, 37077, Göttingen, Germany.
E-mail address: astrid.pundt@kit.edu (A. Pundt).

https://doi.org/10.1016/j.actamat.2019.09.019
1359-6454/

Finally, the steel's ductility in hydrogen environment is reduced [14–18].

While the susceptibility of low-nickel austenitic stainless steels (of the AISI 300 series) to HEE is expected to correlate with the Ni content, detailed studies of the related RRA values reveal the absence of a clear trend [19]. Instead, a broad scatter of the RRA values is observed [5,19,20], ascribed to the complexity of microstructural alterations in steels of different chemical compositions [20,21], where different alloying elements apart from Ni have different tendencies to stabilize or destabilize the austenite phase [22]. Hence, the sole Ni content of the investigated steels cannot be expected to be a sufficient indicator for the steel's HEE [19].

Abstracting from particular alloying elements and considering the probability of martensite formation in tensile tested low-nickel austenitic stainless steels on a wider scope leads to a consistent description of the steel's susceptibility to HEE [5,19]. A linear trend is revealed for a variety of AISI 300 series steels with different chemical compositions, compare Ref. [5], when the probability of deformation-induced martensite formation is expressed by the β-parameter of the Olson-Cohen model [23]. However, some samples fall aside the general trend, which cannot be explained by just referring to the martensite phase, but requires the consideration of other microstructural features of the respective steels.

The present paper aims to identify control parameters that yield reduced HEE of AISI 300 series steels. In this context, the steel's surface oxidation state [14,24] is of particular interest. Different alloying elements show different tendencies to form surface oxides, and different chemical compositions of the steels in general lead to different types of surface oxides [25]. In Ref. [5] we demonstrated that a specific type of surface oxide significantly lowers the steels susceptibility to HEE. Here, we examine this effect in more detail, linking it to microstructural alterations of the steels and the oxide layers in tensile tests. The investigations comprise TOF-SIMS studies of the steel's surfaces combined with microstructural characterizations targeting grain sizes as well as dislocation structures, as determined with TEM. The results are compared to tensile tests of the respective steels in hydrogen atmosphere, as described in Refs. [5,19,26].

2. Experimental

2.1. Materials

Low-Ni content austenitic stainless steels (W11–W21) with chemical compositions given in Table 1 were studied. The chemical compositions of W11 and W12 are close to the standard steels of AISI 304L and 316L, respectively.

Tensile tests were performed on cylindrical rod specimens with gauge lengths of 30 mm and diameters of 5 mm. These were machined from the center of the initial steel bar by wet turning parallel to the rolling direction, reducing the influence of macroscopic alloy segregations on the sample's performance. The rods had a surface roughness of $R_a = 0.38\,\mu m$ [26]. Microstructural characterizations were performed on block or disk shaped specimens. The machining process yields the formation of deformation-induced α′-martensite on the sample surfaces [9]. This was removed by a subsequent solution annealing in vacuum for 30 min at 1050 °C or at 1150 °C, depending on the steel composition (Table 2). In one batch of samples (W11) the influence of the annealing time was also investigated, by reducing it to 15 min. All specimens were quenched in argon (Ar) gas at 200 kPa pressure.

2.2. Oxide layer analysis by TOF-SIMS

The oxide layers formed during the solution annealing process were studied by Time of Flight Secondary Ion Mass Spectrometry (TOF-SIMS IV, ION-TOF GmbH, Münster, Germany) in dual beam mode [27]. Ultra-high vacuum conditions with a background pressure of 1 x 10^{-7} Pa prevent the fresh sample surfaces from oxidation during the time of the analysis. For analysis, negative polarity was applied by using a pulsed Ga^+ beam (25 keV, 0.3 pA) over a 150 × 150μm^2 area which was centered inside a 300 × 300 μm^2 crater. This crater was sputtered by a Cs^+ sputter beam (1 keV, 10 nA). According to the results reported by Asami, a 4 nm oxide layer thickness forms on AISI 304 during wet polishing [28]. Asamis result was adopted here to link the sputter rate to a depth scale, for all samples.

2.3. Tensile tests

Tensile tests were performed at 25 °C (room temperature) or −50 °C in a high purity hydrogen gas (≥99.9999% H_2) atmosphere at 40 MPa and in air at atmospheric pressure, respectively. −50 °C was chosen since HEE of austenitic stainless steels shows a maximum between −50 °C and −70 °C [4]. A constant displacement rate of 0.1 mm/min was applied, resulting in an initial strain rate of $5.5 \times 10^{-5}\ s^{-1}$ according to the standard ASTM-G142-98 for the testing of metals in hydrogen [29]. The relative reduction of area (RRA) was measured ex-situ with a caliper [25], characterizing the susceptibility of a sample to HEE. It is defined as

$$\mathrm{RRA}\ (\%) = \frac{\mathrm{RA}(H_2)}{\mathrm{RA}(\mathrm{air})} \times 100 \qquad (1)$$

An RRA of 100% indicates that there is no influence of hydrogen on the macroscopic tensile ductility of a sample. Martensite transformation curves were determined ex-situ for each steel at −50 °C in air at atmospheric pressure, measuring the martensite content with a Feritscope® MP30 device (Helmut Fischer GmbH, Sindelfingen, Germany) at increments of 5% of engineering strain. For further details see Refs. [5,19,26].

Table 1
Chemical composition of the investigated austenitic stainless steels (wt.%).

Internal Nb.	Material	C	Si	Mn	P	S	Cr	Ni	Mo	Cu	Al	Nb	V	N	B
W11	AISI 304L	0.018	0.69	1.97	0.030	0.030	17.79	8.49	0.29	0.624	0.001	0.01	0.099	0.07	0.0029
W12	AISI 316L	0.012	0.83	1.43	0.030	0.020	17.13	12.24	2.47	0.349	0.002	0.014	0.107	0.057	0.0012
W14	–	0.025	0.02	0.06	0.007	0.006	14.74	10.62	0.02	0.011	1.64	0.01	0.01	0.021	0.001
W15	–	0.013	0.04	0.06	0.005	0.004	14.62	10.83	0.01	0.009	0.001	0.009	0.011	0.146	0.0005
W16	–	0.172	0.05	5.9	0.006	0.008	17.8	7.89	0.02	0.005	0.001	0.003	0.021	0.026	0.0001
W17	–	0.022	0.03	6.04	0.007	0.006	17.28	8.84	0.02	0.006	0.001	0.003	0.011	0.022	0.0164
W18	–	0.099	0.05	0.16	0.006	0.006	14.67	10.96	0.02	0.011	0.009	0.062	0.495	0.014	0.0014
W19	–	0.116	0.05	10.27	0.010	0.005	12.98	7.93	0.03	0.009	2.87	0.008	0.02	0.02	0.0009
W20	–	0.187	0.20	5.57	0.012	0.016	17.91	8.33	2.59	0.128	0.001	0.008	0.031	0.059	0.0008
W21	–	0.147	1.95	9.18	0.008	0.006	14.33	8.43	0.02	0.01	0.001	0.005	0.023	0.035	0.0001

Table 2
Grain sizes and annealing temperatures of the investigated steel samples.

Internal Nb.	Annealing time [min]	Annealing temperature [°C]	Grain size [μm]
W11	15	1050	47(±5)
W11	30	1050	53(±5)
W12	30	1050	42(±5)
W14	30	1050	36(±5)
W15	30	1050	43(±5)
W16	30	1050	38(±5)
W17	30	1050	38(±5)
W18	30	1050	40(±5)
W19	30	1050	39(±5)
W20	30	1150	57(±5)
W21	30	1150	45(±5)

2.4. Dislocation observation by TEM

Transmission Electron Microscope (TEM) observations were conducted with a Philips CM 12 at an acceleration voltage of 120 kV. For these measurements steel specimens with a diameter of 12 mm and a thickness of 1 mm were cut from the initial bar samples. As the outer region of the initial sample contains many defects introduced by the machining process, 3 mm disks were cut at 1 mm distance from the sample edge. Initial thinning was conducted by mechanical polishing. Then, dimpling and Ar ion beam milling were carried out in order to thin down the center of the disk.

3. Results

3.1. RRA values and the probability of strain induced martensite formation

Tensile tests performed at −50 °C on samples that were previously annealed for 30 min reveal a linear correlation of the RRA values with the β-parameter, as shown in Fig. 1. The β-parameter reflects the probability of martensite nucleus formation and is derived from the Olson-Cohen-equation (2) [23]. This equation allows discriminating β- and α-parameters (the latter relates to the rate of sheer band formation) from martensite transformation curves of tensile tested samples, irrespective of the actual chemical composition of a steel sample [5,19]. The linear correlation to the β-parameter is established for a variety of AISI 300 series steels [5]. Hence, the β-parameter occurs to be a reasonable parameter describing HEE of low-nickel austenitic stainless steels. We note that the α-parameters' and other empirical parameters' correlations to HEE of the investigated steels are discussed in detail elsewhere [19].

The martensites' volume fraction $f^{\alpha'}$ as determined with the Feritscope is given by

$$f^{\alpha'} = 1 - exp\{ - \beta[1 - exp(-\alpha\varepsilon)]^n\} \quad (2)$$

with the sample's plastic strain ε and a fixed exponent $n = 4.5$ for austenitic stainless steels. For further details see Ref. [5]. We note that in Fig. 1 data were plotted for the true strain of the samples, yielding more accurate fitting parameters than the engineering strain used in Ref. [5].

Apparently, in Fig. 1 most samples fall onto a straight line, while samples W12 and W17 are clearly departing. In Ref. [5] we broadly attributed these differences to different types of oxide layers present at the sample surfaces. To study the observed effects in more detail, an in-depth analysis of the oxide's topologies was performed, and additional microstructural parameters such as dislocation arrangements and grain sizes were taken into account.

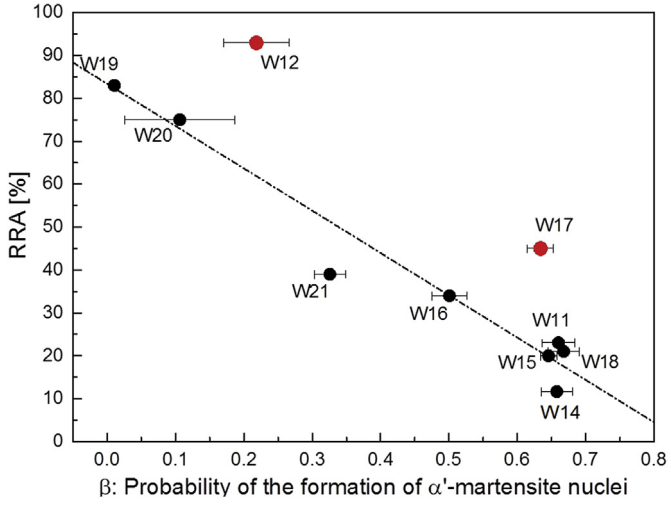

Fig. 1. RRA of the steel samples annealed for 30 min and tensile tested at −50 °C, plotted as a function of the probability β of martensite nucleus formation, as determined by fitting the Olson-Cohen model Equ. (2) to martensite transformation curves [19]. A linear relationship is found for most steels except of the samples W12 and W17. The latter were marked in red. (For interpretation of the references to colour in this figure legend, the reader is referred to the Web version of this article.)

3.2. Oxide layer characterization by TOF-SIMS

TOF-SIMS depth profiles of the oxide layers gathered for the different steels are presented in Fig. 2 for the examples of W14, W16, W17 and W18. The depth profiles show some general features and were classified into four different types regarding the shapes of the profiles [5], subsequently: (a) "thick oxide", (b) "decaying sub-surface oxide", (c) "thin surface oxide" and (d) "high constant level oxide".

The "thick oxide" (a) present for W14 and W19 occurs for those samples containing Al. The "decaying sub-surface oxide" (b), found for W11 (30 min), W16, W20 and W21, shows a gradual decrease of the FeO and the CrO signals to the same intensity level as the Fe_2-signal. The latter reflects the iron signal from bulk. For the "thin surface oxide" (c) of W15 and W18 the signals of FeO and CrO instantly reach the same level as Fe_2 after passing the thin oxide region. For the "high constant level oxide" type (d) of oxides found on W12, W17 and W11 (15 min), the signals of FeO and CrO maintain a constant level, and this level is considerably higher than that of Fe_2. Long depth profile measurements were conducted on W12 and W17. The signals of FeO and CrO in W12 and W17 intersect with Fe_2 at 600 nm and at 1 μm in depth, respectively. It should be noted that the "decaying sub-surface oxide" (b) and the "high constant level oxide" (d) also have a thin surface oxide on top.

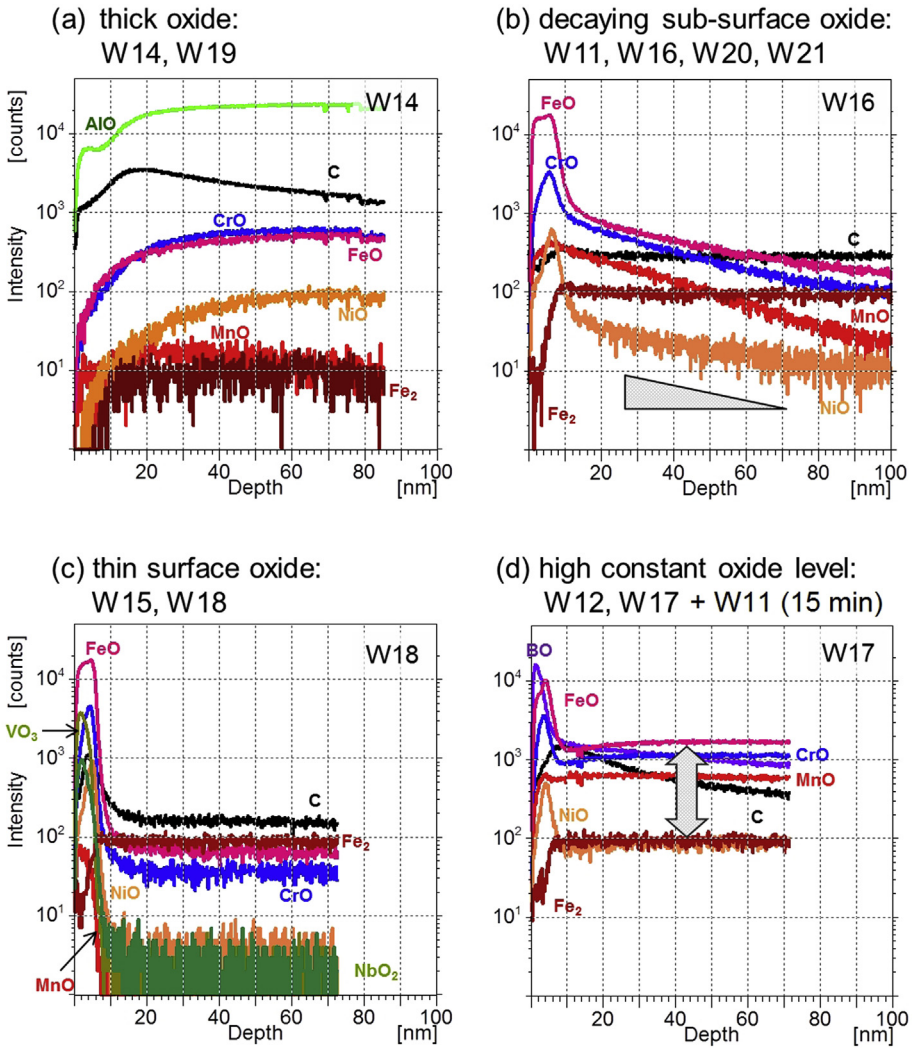

Fig. 2. Types of oxide layers formed on W11–W21 annealed for 30 min. (a) Thick oxide (W14 and W19), (b) decaying sub-surface oxide (W11, W16, W20 and W21), (c) thin surface oxide (W15 and W18) and (d) high constant oxide level (W12 and W17). This type of oxide was also found for W11 annealed for 15 min [5].

As a common feature, an oxide layer stacking comprised of different oxides is found in most of the samples, except for W14 and W19. Alloying elements such as Mo, B, V, Nb and Si are found in the outer layer. The stacking sequence of MnO differs from sample to sample. MnO is found in the outer layer of W11 (30 min), W20 and W21 while a considerably broad profile of MnO was found in W16. Moreover, MnO distributes homogeneously in W12 and W17.

The thick oxide layers of W14 and W19 contain a large amount of AlO. The Al content of W14 and W19 is 1.64 wt% and 2.87 wt%, respectively. The formation of this considerably thick oxide can be explained by selective oxidation. The selective oxidation of aluminum in steel is a well-known phenomenon and often used in high temperature applications [30]. A small amount of Al additive covers the alloy surface in the form of Al-oxide and this dense Al-oxide improves the high temperature corrosion resistance of alloys [30].

For the purpose of comparison, SIMS analysis was conducted on the different alloys in polished condition, as well. Examples of the respective depth profiles, for W14, W16, W18 and W17, are shown in Fig. 3. In all cases, a thin surface oxide layer (3.0–4.5 nm) was observed. After passing the thin surface oxide layer, all oxide signals become lower than the bulk signal of Fe_2. Thus, the oxide types (a) "thick oxide", (b) "decaying sub-surface oxide" and (d) "high constant level oxide" found in Fig. 2 are characteristic of solution annealing, resulting from the migration of metal or oxygen ions in the high temperature oxidation process. In contrast, the "thin surface oxide" (c) is similar to that formed in polished condition. For this type of oxide layer, the only difference between the polished and the solution annealed sample is the thickness of the oxide layer (compare W18 in Fig. 2).

To study the lateral distribution of the element oxides in more detail, representative two-dimensional ion images gathered by TOF-SIMS for the four different groups of oxides are summarized in Figs. 4–7. Further TOF-SIMS maps are presented in the supplemental information.

The SIMS maps were evaluated for different depths below the former sample surfaces, as indicated on the left side of the figures. Integrated signals of FeO, CrO, NiO, MnO, Si and C are shown in depths of 0–10 nm as well as of 40–50 nm for samples with decaying sub-surface oxide (Fig. 5), thin surface oxide (Fig. 6) and high constant level oxide (Fig. 7). For the thick oxide in Fig. 4 the integrated distributions of AlO, FeO, CrO, NiO, MnO and C are presented for the whole oxide thickness.

For all samples except of the samples with the type of thick

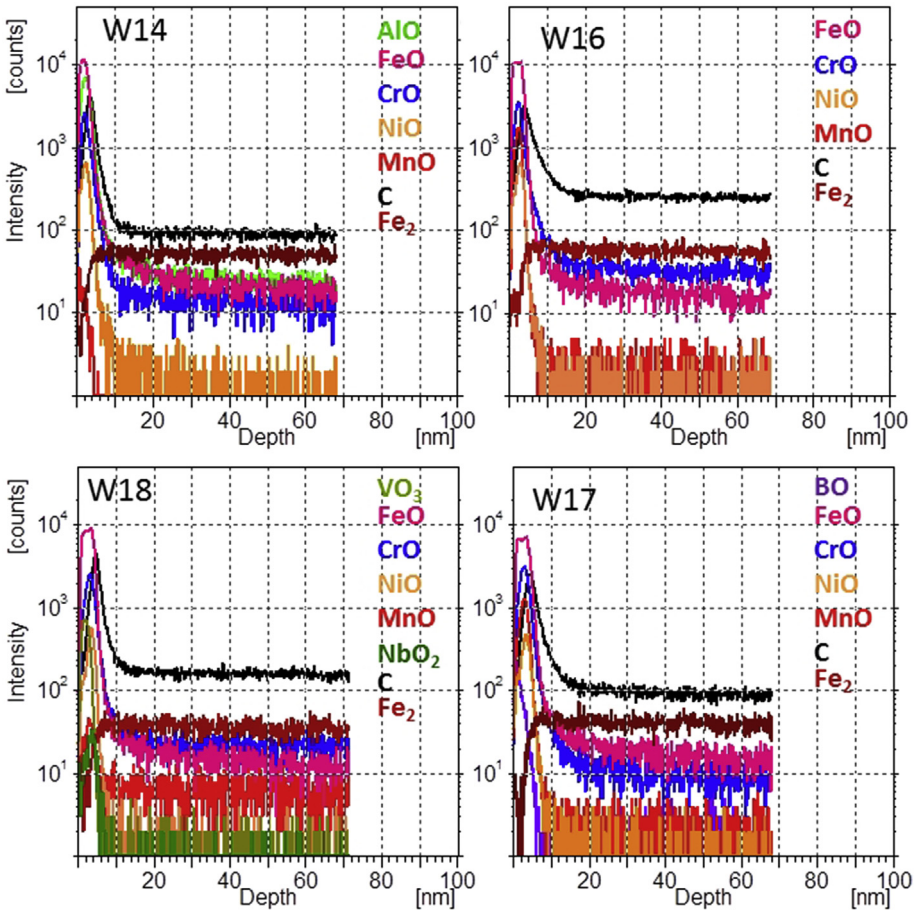

Fig. 3. Oxide layers formed on polished W14, W16, W18 and W17. For all samples, a thin surface oxide is observed.

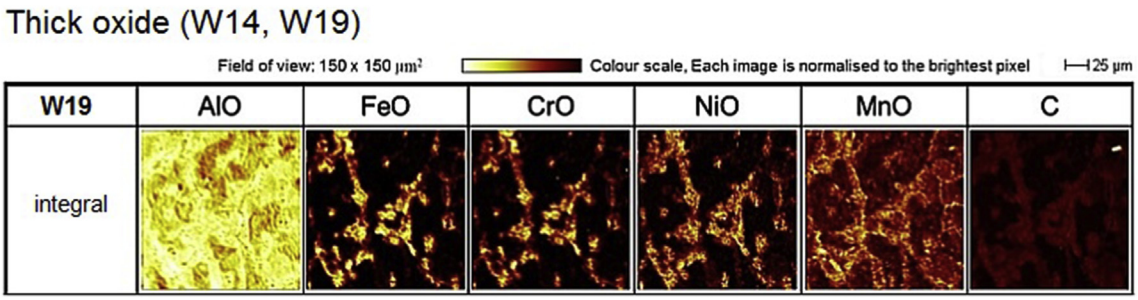

Fig. 4. SIMS maps of different element oxides (AlO, FeO, CrO, NiO, MnO) and C in the "thick oxide" type of steel W19 annealed for 30 min.

oxide layer in Fig. 4 strong differences in the oxide contents are evident between the sample surface (0–10 nm, first row) and the deeper layers of 10 nm width (40–50 nm, second row). As the amount of oxide is given by the colour code, in Figs. 5–7 high oxide contents can be seen on the samples surfaces, in accordance with the depths profiles of Figs. 2 and 3. For example, except for those steels with thick oxides the steels show a strong yellow signal of FeO in the sample's surface layers (first row, left side). Hence, FeO is homogeneously distributed in the upper 0–10 nm depth. In contrast, FeO segregates along grain boundaries in 40–50 nm depth of samples W16, W20 and W21 (see also supplement), yielding yellow lines along the grain boundaries. For most other types of oxides FeO is relatively homogeneous distributed in 40–50 nm depth, as revealed for samples W11, W15, W18, W12 and W17.

Other element oxides such as CrO, NiO, MnO as well as Si and C are differently distributed in lateral directions of the oxide surfaces and in the depths of the oxide layers. For the example of W11 with its decaying sub-surface oxide presented in Fig. 5, CrO, NiO and MnO distribute homogeneously in lateral directions, while Si segregates at grain boundaries. Similar segregation effects are observed for Si in the high constant level oxide of W12 in Fig. 7. By contrast, in W12 CrO and MnO are strongly enriched on the surface of some grains, yielding an inhomogeneous lateral distribution in the uppermost 10 nm layer (first row). These grain-dependent oxide intensity levels suggest a grain orientation dependency of the oxide layer thickness. The thickness of these strong oxide

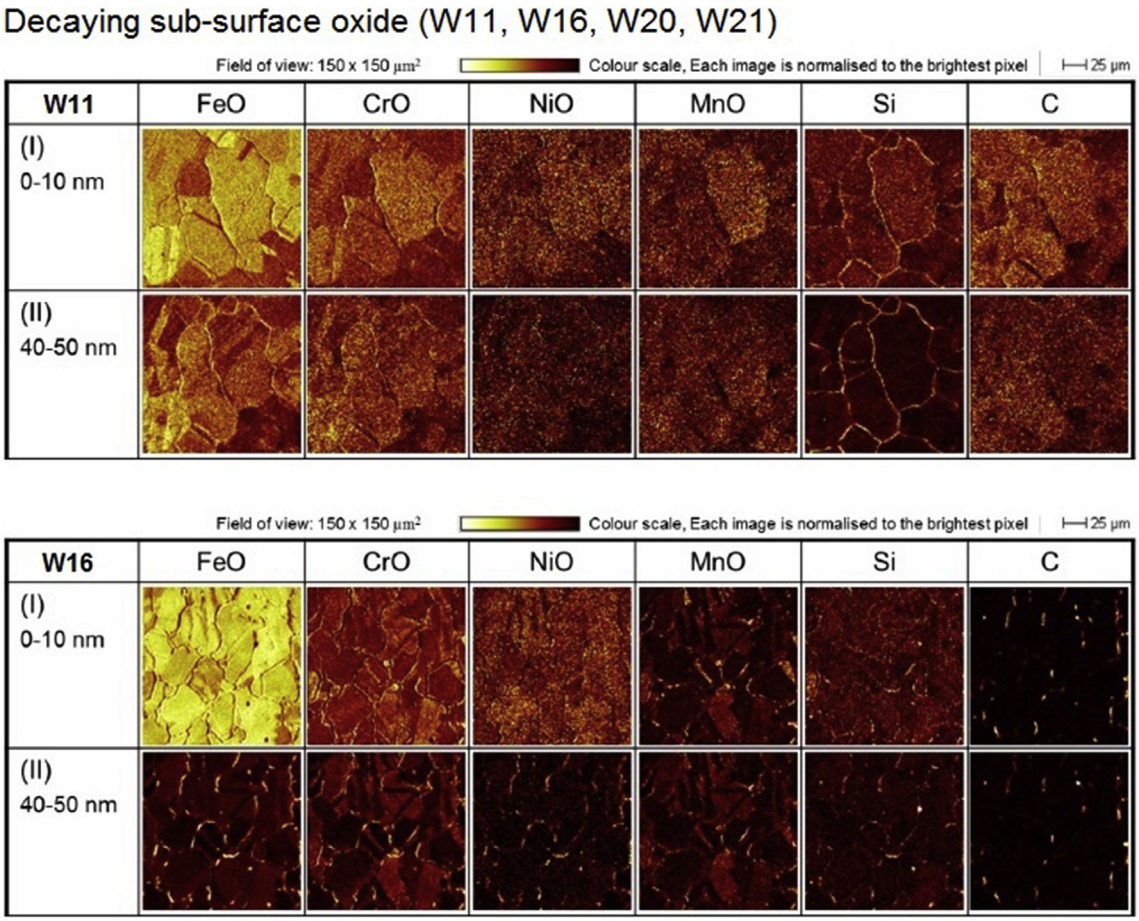

Fig. 5. SIMS maps of steels with "decaying sub-surface oxides" W11 and W16. The distribution of FeO, CrO, NiO, MnO, Si and C is shown for the uppermost surface region (0–10 nm depth) of the oxide layer, and for a depth of 40–50 nm.

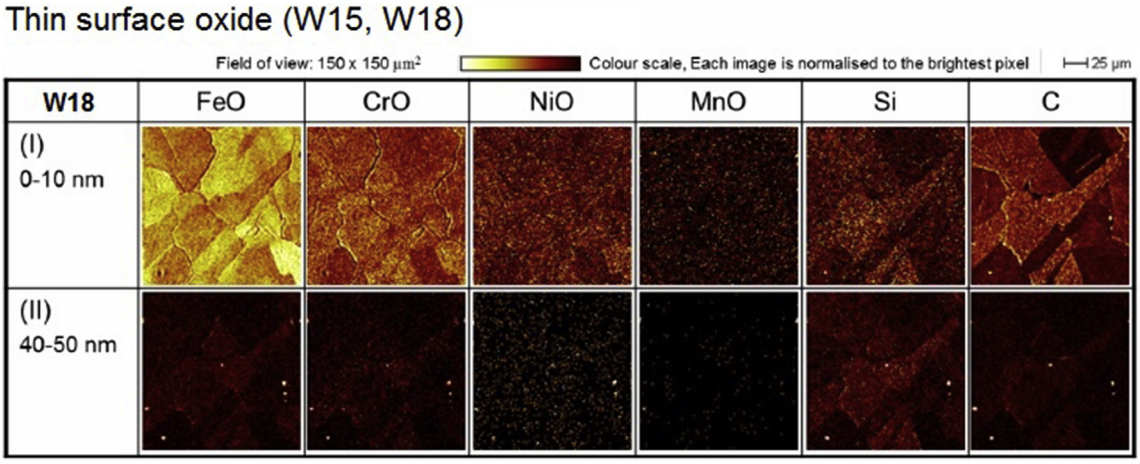

Fig. 6. SIMS maps of the "thin surface oxide" of steel W18. The oxide layer is mainly restrained to the first 10 nm depth.

enrichments is below 10 nm, resulting in ion image colour variation.

In the thick oxide of W19 with its homogeneous oxide depth distribution in Fig. 4, AlO is homogeneously distributed in lateral directions, while FeO, CrO, NiO, MnO and C clearly segregate in distinguished regions. A more in-depth analysis of these enrichments reveals that the oxides apart from AlO are co-localized in small particles, that are deficient of AlO. For details see Ref. [25]. Such particular enrichments have not been observed in the thick oxide of W14 (see supplement) or in the other types of oxides.

To give a systematic overview of the different oxide types'

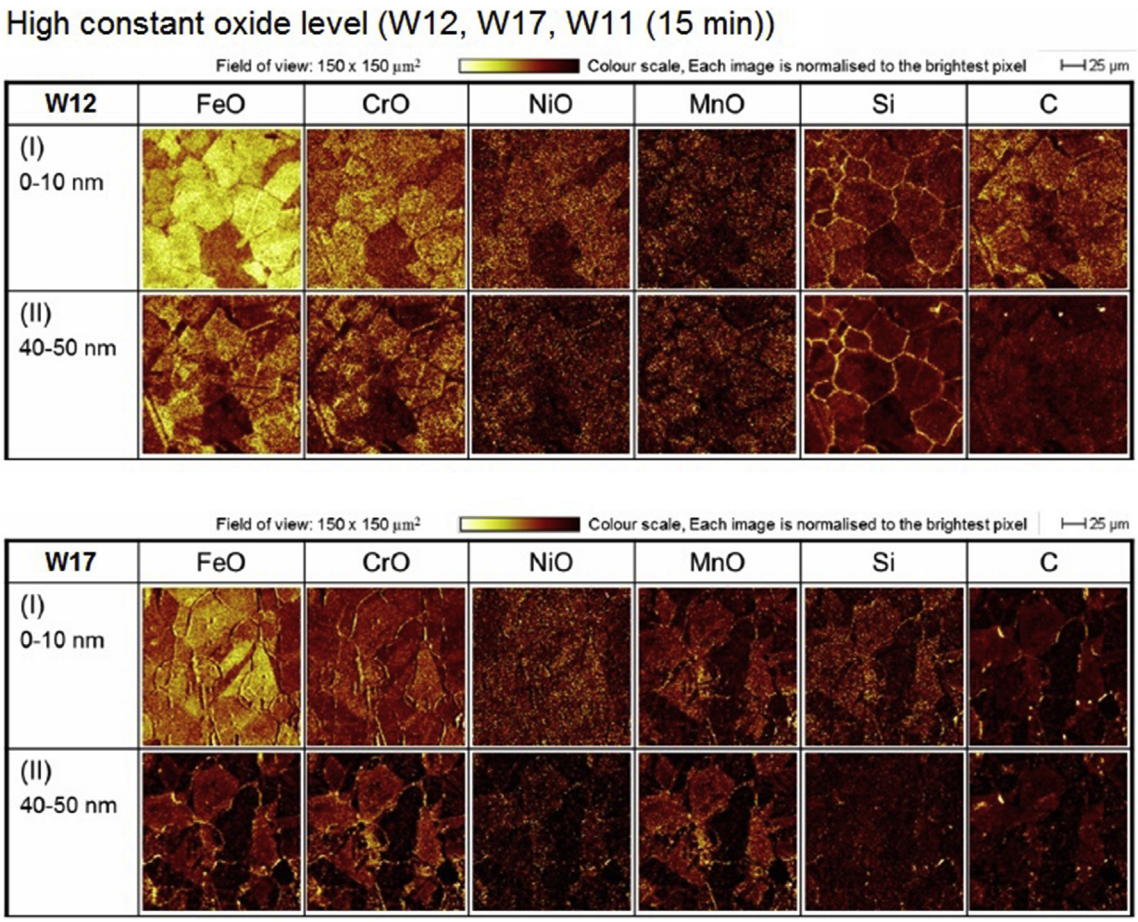

Fig. 7. SIMS maps of the steels with "high constant level oxides" W12 and W17.

characteristics, in Fig. 8 three-dimensional schematic illustrations of the oxide layers are presented. In type (a), the "thick oxide", all elements are relatively homogeneously distributed in case of the 900 nm thick oxide of W14, while in case of the 150 nm thick oxide of W19 FeO, CrO, NiO, MnO and C are co-segregated, forming a laterally island-like pattern. For type (b), the "decaying sub-surface oxides", segregations of Si (for W11) and of FeO, CrO, NiO, MnO as well as Si and C at grain boundaries in the sub-surface region are found in the 100 nm thick oxide layers. In case of type (c), the "thin surface oxides", a layer of approx. 10 nm thickness is present. The oxides do not significantly segregate at grain boundaries. They are homogeneously distributed in surface and sub-surface regions. For the case of type (d), the "high constant level oxide", the pattern of oxides such as FeO, CrO, NiO and MnO is related to the grain structure for W12 and W17 throughout the oxide layer, while a localized enrichment of the oxides at triple junctions of grains is observed for W11 (15 min). Further details of the oxide layer structures are given in Ref. [25] and in the supplemental information.

Oxide effects on HEE may be interfered by other microstructural parameters. This is suggested by the specimens of batch W11, that were annealed for 15 or 30 min, respectively, and tensile tested at room temperature. While W11 (15 min) revealed a relative reduction of area of RRA = 82%, W11 (30 min) showed RRA = 51%, see Ref. [5]. Next to the different types of oxides found for these samples (Figs. 2, 5 and 8 and supplemental information), these differences might be related to grain size effects or different arrangements of dislocations in samples with different annealing times. These aspects are considered subsequently.

3.3. Dislocation structures

Dislocation arrangements were analyzed by TEM for the model steel W11. TEM micrographs of this steel are shown in Fig. 9. Fig. 9 (a, b) shows the bulk state in the as-received, hot rolled condition. Fig. 9 (c, d) shows the state after solution annealing for 15 min, and (e, f) after solution annealing for 30 min, each at different magnifications. The TEM samples are taken from an inner position of the original sample, as described in section 2.4. Therefore, the observed microstructure does not reflect defects introduced by the machining process but results from the rolling and quenching process. In the as-received state (a, b) deformation bands are found as indicated by red arrows. Furthermore, the dislocation density in the as-received state is higher than that of W11 when annealed for 15 min and 30 min (c-f).

Focusing on the dislocation arrangement, dislocation tangles are observed in the as-received state (a,b). The dislocations locally tangle when W11 is annealed for 15 min (c, d), but on a larger scale the observed dislocations align in a grid-like fashion. In W11 annealed for 30 min (f), dislocations pile-up at grain boundaries. The dislocations are observed to occur parallel to each other.

3.4. Grain sizes

The grain size of the steels was measured on polished bar samples by means of optical microscopy. To enhance the optical

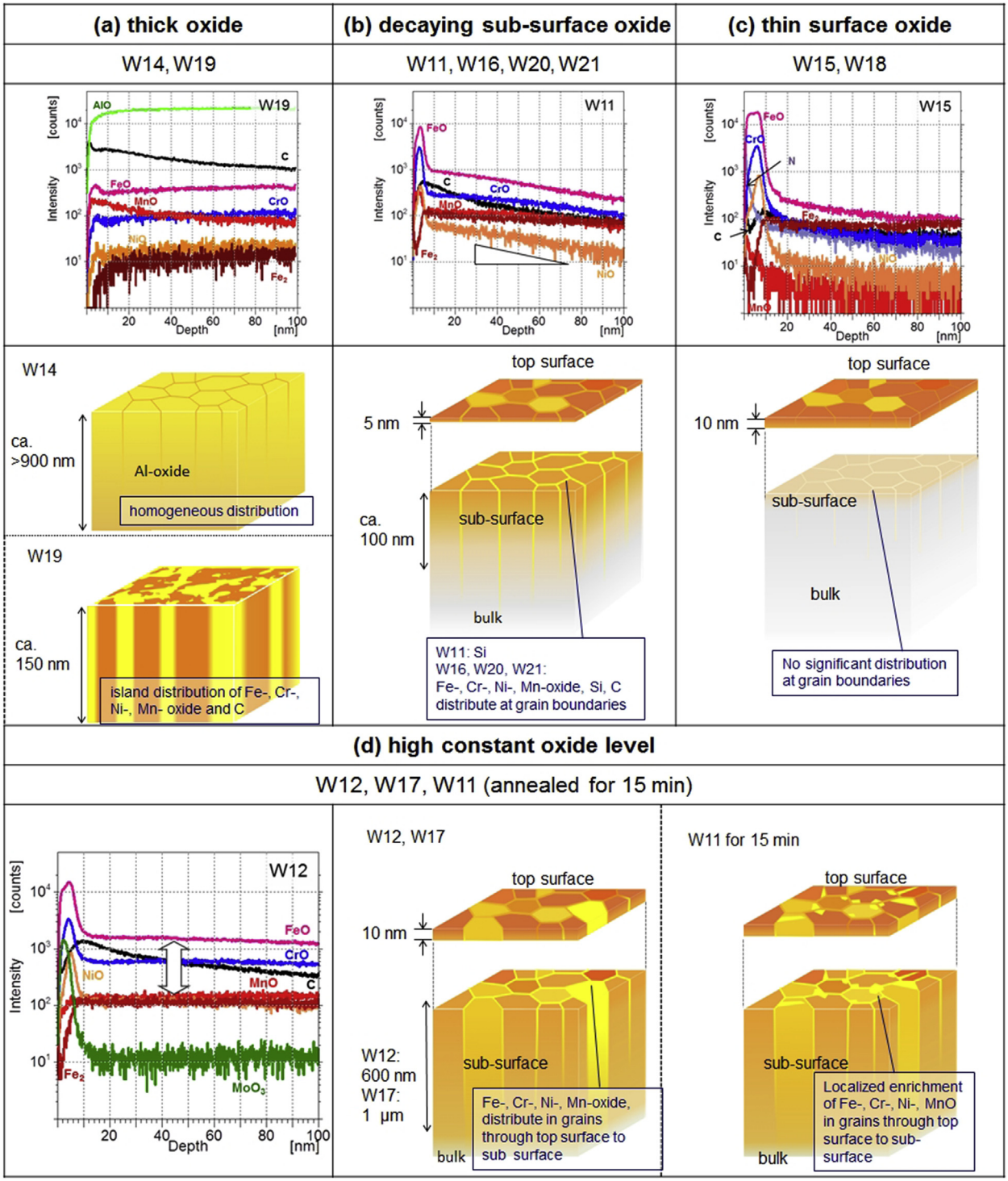

Fig. 8. Summary of oxides found in the surfaces of the steels investigated in this study.

contrast the sample surfaces were etched in V_2A solution (100 ml H_2O, 100 ml HCl, 10 ml HNO_3) [9]. Resulting grain sizes are summarized in Table 2.

4. Discussion

4.1. Oxide layer influence

In Fig. 1, a general trend line of RRA(β) is established for most samples annealed for 30 min and tensile tested at −50 °C. But, HEE of samples W12 and W17 is significantly reduced. We note that similar behaviour is observed when the empirical M_{d30} temperature (Nohara, [31]) of the samples is taken into account instead of the probability β of martensite nucleation, see Ref. [19]. In particular, for W12 and W17 the type of "high constant level oxide" was found in Fig. 2, which differs principally from the other, mainly decaying types of oxides. Therefore, next to other factors such as dislocation structures and grain sizes, the different performance of

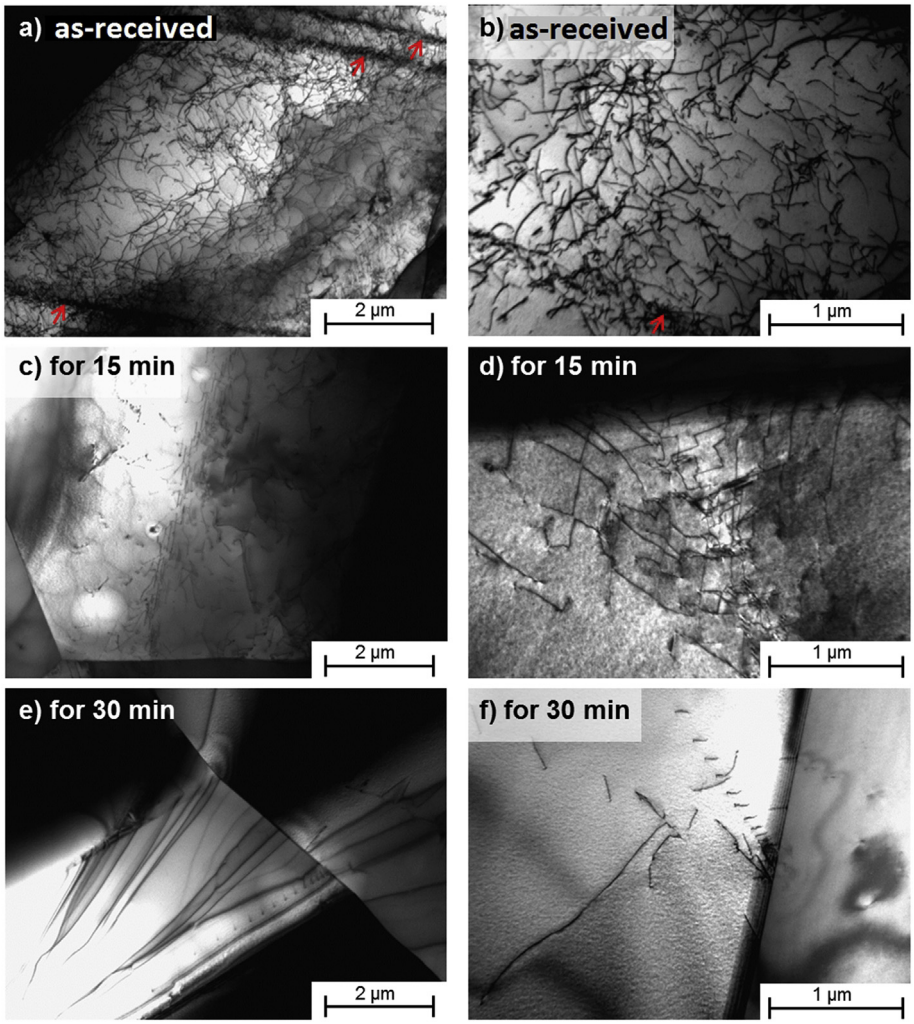

Fig. 9. Microstructure of the bulk of alloy W11 (a),(b) in the as-received state; (c),(d) solution annealed for 15 min; (e), (f) solution annealed for 30 min, at different magnifications. (a, b): Deformation bands indicated by red arrows and dislocation tangles are observed in the as-received state. (c–f): The dislocation density is low for W11 annealed for 15 min and 30 min, while it is reduced by one order of magnitude in W11 (30 min) compared to W11 (15 min) [25]. Dislocation pile-ups at grain boundaries can be observed in (f). (For interpretation of the references to colour in this figure legend, the reader is referred to the Web version of this article.)

W12 and W17 can be linked to the special type of the oxide layer. The same type of oxide was found for sample W11 when annealed for 15 min, while W11 annealed for 30 min has a decaying subsurface oxide, see Fig. 2. Intriguingly, the relative reduction of area (RRA) of W11 (15 min) is 60% larger at room temperature compared to that of W11 (30 min). However, the dislocation patterns of these samples are different as well, see Fig. 9. Therefore, possible interfering effects of dislocation arrangements onto RRA will be discussed below.

Oxides often act as protective layers with respect to the hydrogen permeation into steels, since it is assumed that they prevent the dissociation of hydrogen molecules or prevent hydrogen diffusion. However, during tensile tests the oxide layers crack due to sample elongation. Thereafter, dissociation of hydrogen molecules can occur on freshly created steel surfaces [32], while the remaining oxide only limits the surface area available for hydrogen entry.

Regarding their mechanical properties, oxides are inherently brittle. The thermal expansion of oxides is smaller than that of metals, resulting in local elastic compression in the oxides and tension in the metals during the cooling process prior to tensile tests [33]. This may lead either to a brittle fracture or spalling of the oxide layer during subsequent tensile tests. However, the oxide thickness and the external strain strongly influence the failure mode of the oxide layers, since brittleness is regarded as a size-dependent feature [34].

The failure map, representing the failure strain as a function of oxide thickness, indicates that a thin oxide layer of less than several hundred nanometers fails in a ductile manner [34]. Thus, from a general point of view the deformation mode of the studied oxide layers matches that of the bulk metal in the early stages of tensile testing. However, in this context also the ratio of specimen elongation and oxide layer thickness has to be considered. Strain rates of $5.5 \times 10^{-5}\,s^{-1}$ at gauge lengths of 30 mm applied in this study yield a cross-head displacement rate corresponding to specimen elongation of $1.65\,\mu m\,s^{-1}$. At this displacement rate oxide layers of types (b) and (c), which are 5 nm–100 nm thick, break within some seconds, according to the strain-thickness failure maps of Robertson et al. [34]. Then, hydrogen can enter through the fresh surface, and the cracks formed in the oxide layer can grow into the metal in the proceeding test.

Contrariwise, the (d)-types of oxide layers continue to a depth of 600 nm to 1 µm. This type of oxides may, therefore, suppress the hydrogen entry even though it is partially cracking at the early

stages of tensile testing. Next to the passivating effect of oxide layers and mechanical cracking, crack formation and propagation will depend on the oxide's spatial distribution in and on the metal matrix. Here, three effects need to be considered, while two of them are counteracting, complicating the interpretation of the oxide's influence. First, lateral enrichments of oxides in triple junctions, such as on W11 (15 min), might act as obstacles that block crack propagation [4,35], reducing HEE. Second, at obstacles dislocation motion will be impeded, and dislocation pile-ups occur. This leads to stress concentrations and the emergence of dislocation sources at these sites [36,37], yielding enhanced embrittlement. Third, the stacked structure of the oxide layers with a region enriched of FeO at the outer oxide surface for oxides of type (b) – (d) might be of importance, since it can alter crack propagation into the sample.

This could account for the performance of W12 and W17, where the element oxides show only small lateral segregation effects. In W11 (15 min), however, the stacking tendency is lower; here the relative oxide thickness and the crack stopping at obstacles might dominate.

The thick homogeneous aluminum oxide of W14, on the other hand, might be too homogeneous to affect crack propagation. Notably, W19 with its thick aluminum oxide layer and strongly segregated other element oxides is of a different case. For W19, tensile tests performed with the thick aluminum oxide layer yield almost the same RRA values compared to samples, where the oxide layer was removed prior to tensile tests [26]. Consequently, the thick aluminum oxide of W19 does not seem to act as a protecting layer against hydrogen entry.

In total, regarding the crack propagation behaviour in oxide layers more research is required, while the results of the present study suggest that a lateral enrichment of oxides and/or a stacked oxide structure reduce HEE.

4.2. Influence of grain sizes and dislocation arrangements

Only a few studies are available considering grain size effects on HEE [35–40]. Moody et al. investigated the effect of hydrogen on the fracture toughness of the Fe–Ni–Co superalloy IN903 (austenite) with grain sizes ranging from 28 to 200 μm [38]. They found that the effect of hydrogen on the fracture toughness of pre-charged samples was independent of the grain size. In contrast, Eliezer et al. reported that the resistance of austenitic stainless steels (AISI 304L, 316L, 316, 321 and 347) to HEE, that were cathodically charged during tensile tests, improves by decreasing the grain size [39,40]. Recently, Weber et al. [35] investigated the effect of grain sizes on the formation of strain-induced α'-martensite and HEE of AISI 304L at room temperature. They found that samples of 13 μm (polished) yield higher RRA values than 130 μm (polished), indicating a better HEE resistance for smaller grain size. First, as shown by Jun et al. [41], for smaller grain sizes below a threshold value of 35 μm the austenite stability is enhanced due to increased stacking fault energies. Second, the enhancement of fine grained steel's ductility can again be attributed to grain boundaries and segregation bands acting as obstacles to stop the growth of hydrogen-assisted cracks [35].

In the present study, the grain sizes of all samples were above the threshold value reported by Jun et al. [41], and with 36–57 μm they were all similar (Table 2). Therefore, grain size effects are expected to be small, here. This is especially revealed by the alloy W11 annealed for 15 min and 30 min, respectively. There, the effect of heat treatment time on the grain size is insignificantly small, since the grain size in both samples was found to be almost identical with 47 μm (15 min) and 53 μm (30 min), respectively. Although the higher RRA was recorded for the finer grain size, the scale of the effect indicates that grain size is not a dominant factor in the observed HEE.

Taking dislocation effects on HEE in tensile tests into consideration, we here refer to the HELP theory of hydrogen enhanced local plasticity [42,43]. HELP predicts the enhancement of dislocation motion in the presence of hydrogen, leading to HEE of steels. This effect is expected to increase with increasing dislocation density. Enhanced dislocation densities in the parent austenite phase might further increase the driving force for the growth of martensite nuclei, due to the austenite's work hardening with an increase of its shear strength [44]. Regardless of the different types of oxide layers found for the samples, from this point of view it would be expected that W11 annealed for 30 min was less susceptible to HEE than W11 annealed for 15 min, because longer annealing time reduces the dislocation density by one order of magnitude [25]. However, this is in contrast with the actual performance of the samples.

From geometric arguments, the higher RRA value for the sample annealed for 15 min can be interpreted in terms of the dislocation substructures found in Fig. 9. Louthan et al. investigated the effects of the high energy rate forging (HERF) process on HEE [16], resulting in dislocation tangles and cell structures in austenitic stainless steels without the formation of a martensite phase. The heavily deformed specimens of Louthan et al. were pre-charged in 69 MPa hydrogen gas at elevated temperatures of 100–200 °C, and subsequently tensile tested in air at room temperature. They reported a 68% reduction in area (RA) observed in HERFed AISI 304L steels as compared to 36% RA in annealed AISI 304L steels [16], yielding an improved resistance to HEE of AISI 304L by the HERF process (prior to hydrogen charging). This is ascribed to dislocation tangles and cellular structures impeding the hydrogen transport by dislocation motion [16].

As shown in Fig. 9 (d) and (f), dislocation tangles are partially observed in W11 when annealed for 15 min, while only some dislocations aligned in parallel remain in W11 when annealed for 30 min. It is therefore possible that the higher RRA value of W11 (15 min) results from restrained dislocation motion due to the dislocation tangles and cellular structures [16]. However, on a closer look the dislocation substructures observed in W11 (15 min) differ from Louthan's study, as they are much less pronounced. Cellular dislocation structures are not very evidently seen in Fig. 9 (c, d), and dislocation tangles are only partially observed. In contrast, HERFed AISI 304L shows a strong cellular dislocation structure in Ref. [16].

Caution should be further exercised, since a later study by West [36] suggested that the HERF process improves the resistance to HEE only in the pre-charged condition. Under tensile tests at high hydrogen pressures in the range from 69 to 173 MPa, HERFed steels were severely embrittled compared to annealed steels, and the degree of embrittlement increased with increasing hydrogen test pressure [36]. This means that at high hydrogen pressures dislocation tangles and cellular dislocation structures do not have any beneficial or even have a detrimental effect in minimizing the susceptibility of steels to HEE.

In the present study, tests were carried out at 40 MPa hydrogen pressure. This pressure is lower than that used by West et al., but in the light of the above arguments an extrapolation from 69 MPa to 40 MPa predicts that dislocation structures do not play a significant role in resistance to HEE of W11. In total, the impact of HERF and related dislocation substructures is still an open question. Further investigations on the effect of dislocation structures on HEE are required.

Finally, we conclude that the main effects of improved HEE resistances of W11 (15 min), W12 and W17 are related to their special type of “high constant level oxide”, while effects of grain sizes and dislocation structures are of minor importance, here. The other

types of oxides on the other steel samples are either too thin to inhibit hydrogen entry into the steel, as they are cracking, or they do not act as passivating layers, as suggested in case of thick aluminum oxide.

5. Summary

In the present study we investigated the impact of surface oxide layers, dislocation arrangements and grain sizes on the HEE susceptibility of low-nickel austenitic stainless steels. Grain sizes and dislocation structures turned out to be of minor importance in HEE, here. The differences in grain sizes for the different steels investigated were too small to yield considerable effects, and dislocation substructures such as tangle dislocations or cell structures were not established clear enough to influence the hydrogen-dislocation interaction in a different way.

It was demonstrated that the effect of the oxide layers on HEE strongly depends on the oxide's depth profiles. The oxides were categorized into four different types (a)-(d), depending on their depth profile. For the types of (a) “thick oxide”, (b) “decaying subsurface oxide” and (c) “thin surface oxide”, the oxide layers play a secondary role in HEE. They either crack, forming fresh steel surfaces in tensile tests, or they do not act as passivating layers, hindering the dissociation of hydrogen molecules at the steels' surfaces. But, the specific type of oxide layer (d), the “high constant level oxide”, improves the resistance of steels to HEE by approximately $\Delta RRA = 25\%$. Expanding the beneficial effects proposed in Ref. [5], this type of oxide might not to crack completely in early stages of tensile tests. This effect might be related to the oxide layer stacking or local enrichments of oxides at grains and triple junctions, acting as obstacles for the propagation of cracks. It could reduce the hydrogen permeation into the steel and might be utilized in applications.

Associated content

Supplemental information is provided for SIMS maps of the three-dimensional element oxide distribution in steel samples investigated in this study.

Acknowledgment

The authors gratefully acknowledge financial support of the Bundesministerium für Wirtschaft und Technologie (BMWi) within the project 0327802C and the Deutsche Forschungsgemeinschaft (DFG) via PU 131/9-1/2 and WE 4435/4-1.

Appendix A. Supplementary data

Supplementary data to this article can be found online at https://doi.org/10.1016/j.actamat.2019.09.019.

References

[1] W.T. Chandler, R.J. Walter, Effects of high pressure hydrogen on metals at ambient temperature. NASA-CR-102425, R-7780-1, Rocket Calif (1969).
[2] S. Fukuyama, L. Zhang, K. Yokogawa, Development of materials testing equipment in high pressure hydrogen and hydrogen environment embrittlement of austenitic stainless steels, J Japan Inst Met 68 (2004) 62.
[3] L. Bracke, L. Kestens, Penning Transformation mechanism of α′-martensite in an austenitic Fe–Mn–C–N alloy, J. Scr Mater 57 (2007) 385.
[4] T. Michler, A. Yukhimchuk, J. Naumann, Hydrogen environment embrittlement testing at low temperatures and high pressures, Corros. Sci. 50 (2008) 3519.
[5] C. Izawa, S. Wagner, M. Martín, S. Weber, R. Pargeter, T. Michler, H.H. Uchida, A. Pundt, SIMS analysis on austenitic stainless steel: the influence of type of oxide surface layer on hydrogen embrittlement, J Alloys Compd 580 (2013) S13.
[6] I. Altenberger, B. Scholtes, U. Martin, H. Oettel, Cyclic deformation and near surface microstructures of shot peened or deep rolled austenitic stainless steel AISI 304, Mater. Sci. Eng. A 264 (1999) 1.
[7] T. Michler, C. San Marchi, J. Naumann, S. Weber, M. Martin, Hydrogen environment embrittlement of stable austenitic steels, Int J Hydr En 37 (2012) 16231.
[8] T.P. Perng, C.J. Altstetter, Comparison of hydrogen gas embrittlement of austenitic and ferritic stainless steels, Metall Trans A 18 (1987) 123.
[9] M. Martín, S. Weber, C. Izawa, S. Wagner, A. Pundt, W. Theisen, Influence of machining-induced martensite on hydrogen-assisted fracture of AISI type 304 austenitic stainless steel, Int. J. Hydrogen Energy 36 (2011) 11195.
[10] Y. Mine, C. Narazaki, K. Murakami, S. Matsuoka, Y. Murakami, Hydrogen transport in solution-treated and pre-strained austenitic stainless steels and its role in hydrogen-enhanced fatigue crack growth, Int. J. Hydrogen Energy 34 (2009) 1097.
[11] H. Bhadeshia, R. Honeycomb, Steels: Microstructure and Properties, Butterworth-Heinemann, 2017.
[12] R. Kirchheim, Reducing grain boundary, dislocation line and vacancy formation energies by solute segregation. I. Theoretical background, Acta Mater. 55 (2007) 5129.
[13] R. Kirchheim, Revisiting hydrogen embrittlement models and hydrogen-induced homogeneous nucleation of dislocations, Scr. Mater. 62 (2010) 67.
[14] C. San Marchi, B.P. Somerday, X. Tang, G.H. Schiroky, Effects of alloy composition and strain hardening on tensile fracture of hydrogen-precharged type 316 stainless steels, Int J Hydr En 33 (2008) 889.
[15] T.L. Capeletti, M.R. Louthan, J the tensile ductility of austenitic steels in air and hydrogen, Eng Mater Technol 99 (1977) 153.
[16] M.R. Louthan, G.R. Caskey, J. Donovan, D. Rawl, Hydrogen embrittlement of metals, Mater. Sci. Eng. 10 (1972) 357.
[17] J.A. Brooks, A.J. West, Hydrogen induced ductility losses in austenitic stainless steel welds, Metall Trans A 12 (1981) 213.
[18] C. San Marchi, B.P. Somerday, X. Tang, G.H. Schiroky, Hydrogen assisted fracture of type 316 stainless steel at sub-ambient temperature, in: Proc. PVP2008 2008 ASME Press. Vessel. Pip. Div. Conf. July 27-31, 2008, ASME, Chicago, Illinois, USA, 2008.
[19] C. Izawa, S. Wagner, M. Deutges, M. Martin, S. Weber, R. Pargeter, T. Michler, H.H. Uchida, R. Gemma, A. Pundt, Relationship between hydrogen embrittlement and M_{d30} temperature: prediction of low-nickel austenitic stainless steel's resistance, Int. J. Hydr. En. 44 (2019) 25064–25075.
[20] G. Egels, L. Mujica Roncery, R. Fussik, W. Theisen, S. Weber, Impact of chemical inhomogeneities on local material properties and hydrogen environment embrittlement in AISI 304L steels, Int. J. Hydr. En. 43 (2018) 5206–5216.
[21] R. Fussik, S. Weber, Local microstructural stability and hydrogen embrittlement of iron-base FCC alloys, J. Mater. Sci. Eng. A 6 (2016) 243–253.
[22] A.L. Schaeffler, Constitution diagram for stainless-steel weld metal. 2. Schaeffler diagram, Met Prog 106 (1974) 227.
[23] G.B. Olson, M. Cohen, Kinetics of strain-induced martensitic nucleation, Metall Trans A 6 (1975) 791.
[24] H.H. Uchida, E. Fromm, Kinetics of hydrogen absorption of titanium/metal (vanadium, chromium, manganese, iron, nickel) sandwich films with and without oxygen precoverage at 300 K, J Less Com Met 131 (1987) 125.
[25] C. Izawa, Extended TOF-SIMS Analysis on Low-Nickel Austenitic Stainless Steels: the Influence of Oxide Layers on Hydrogen Embrittlement, Göttingen university, 2015. Dissertation thesis, http://hdl.handle.net/11858/00-1735-0000-0028-8693-0.
[26] M. Martín, Development of Lean Alloyed Austenitic Stainless Steels with a High Resistance to Hydrogen Environment Embrittlement, PhD Thesis, Eigenverlag des Lehrstuhls Werkstofftechnik der Ruhr-Universität Bochum, 2012, ISBN 978-3-943063-09-7.
[27] K. Iltgen, Optimized time-of-flight secondary ion mass spectroscopy depth profiling with a dual beam technique, J Vac Sci Technol A Vacuum, Surfaces, Film 15 (1997) 460.
[28] K. Asami, K. Hashimoto, S. Shimodaira, XPS determination of compositions of alloy surfaces and surface oxides on mechanically polished iron-chromium alloys, Corros. Sci. 17 (1977) 713.
[29] G142-98, Standard Test Method for Determination of Susceptibility of Metals to Embrittlement in Hydrogen Containing Environments at High Pressure, High Temperature, or Both, ASTM International, West Conshohocken, 2004, 2004.
[30] F.H. Stott, G.C. Wood, J. Stringer, The influence of alloying elements on the development and maintenance of protective scales, Oxid Met 44 (1995) 113.
[31] K. Nohara, Y. Ono, N. Ohashi, Composition and grain size dependencies of strain-induced martensitic transformation in metastable Austenitic stainless, Tetsu to Hagane 63 (1977) 772.
[32] M. Cacciatore, G.D. Billing, Dissociation and atom recombination of H2 and D2 on metallic surfaces: a theoretical survey, Pure Appl. Chem. 68 (1996) 1075.
[33] B. Pieraggi, R.A. Rapp, Stress generation and vacancy annihilation during scale growth limited by cation-vacancy diffusion, Acta Metall. 36 (1988) 1281.
[34] J. Robertson J, M.I. Manning, Limits to adherence of oxide scales, Mater. Sci. Technol. 6 (1990) 81.
[35] S. Weber, M. Martín, W. Theisen, Impact of heat treatment on the mechanical properties of AISI 304L austenitic stainless steel in high-pressure hydrogen gas, J. Mater. Sci. 47 (2012) 6095.
[36] A.J. West, M.R. Louthan, Dislocation transport and hydrogen embrittlement, Metall Trans A 10 (1979) 1675.

[37] K.A. Nibur, B.P. Somerday, D.K. Balch, C. San Marchi, The role of localized deformation in hydrogen-assisted crack propagation in 21Cr–6Ni–9Mn stainless steel, Acta Mater. 57 (2009) 3795.
[38] N.R. Moody, R.E. Stoltz, M.W. Perra, The effect of hydrogen on fracture toughness of the Fe-Ni-Co superalloy IN903, Metall Trans A 18 (1987) 1469.
[39] E. Minkovitz, D. Eliezer, Grain-size and heat-treatment effects in hydrogen-assisted cracking of austenitic stainless steels, J. Mater. Sci. 17 (1982) 3165.
[40] P. Rozenak, D. Eliezer, Effects of metallurgical variables on hydrogen embrittlement in AISI type 316, 321 and 347 stainless steels, Mater. Sci. Eng. 61 (1983) 31.
[41] J.H. Jun, C.S. Choi, Variation of stacking fault energy with austenite grain size and its effect on the MS temperature of γ->ε martensitic transformation in Fe–Mn alloy, Mater. Sci. Eng. A 257 (1998) 353.
[42] H.K. Birnbaum, P. Sofronis, Hydrogen-enhanced localized plasticity—a mechanism for hydrogen-related fracture, Mater. Sci. Eng. A 176 (1994) 191.
[43] P. Sofronis, H.K. Birnbaum, Mechanics of the hydrogen - dislocation - impurity interactions—I. Increasing shear modulus, J. Mech. Phys. Solids 43 (1995) 49.
[44] E. Breinan, G. Ansell, The influence of austenite strength upon the austenite-martensite transformation in alloy steels, OR Trans. 1 (1970) 1513.